RSC Advances

PAPER

View Article Online
View Journal | View Issue

Check for updates

Cite this: *RSC Adv.*, 2026, **16**, 246

Understanding the charge-storage mechanism and interfacial kinetics of graphitic carbon nitride electrodes in redox-additive electrolytes for supercapacitors

Mustapha Balarabe Idris, * Bhekie B. Mamba and Fuku Xolile

Received 24th November 2025
Accepted 14th December 2025

DOI: 10.1039/d5ra09074a

rsc.li/rsc-advances

The addition of a redox additive to an aqueous electrolyte is one of the facile methods to enhance the electrochemical performance of carbon-based electrode materials. Furthermore, understanding the mechanisms and charge-transfer kinetics at electrode/electrolyte interfaces provides invaluable information, which enables the rational design of interfaces between the electrode and the electrolyte, thereby achieving optimal performance. Herein, we report the role of redox additives, namely, H_2SO_4 + $K_3Fe(CN)_6$ and H_2SO_4 + KI, in enhancing the capacitance performance of carbon-rich graphitic carbon nitride (CR-gCN). The cyclic voltammetry and galvanostatic charge–discharge revealed that CR-gCN exhibited superior charge storage in H_2SO_4 + KI, which is ~3.5-fold higher than in pristine H_2SO_4 electrolyte. Although charge storage mechanism studies revealed that a diffusion-controlled process dominates the capacitance contribution in both electrolytes at lower scan rates, the H_2SO_4 + KI electrolyte shows a greater diffusive contribution at higher scan rates, indicating faster ion transport from the bulk to the electrode interfacial region. The charge transfer kinetics of CR-gCN in redox additive electrolytes investigated using modified Nicholson's method reveal that H_2SO_4 + KI electrolyte exhibits a heterogeneous charge transfer constant (k^0_{eff}) of 0.453 cm s^{-1}, which is approximately 1.6 times higher than that of H_2SO_4 + $K_3Fe(CN)_6$, suggesting faster interfacial electron transfer. A symmetric device fabricated using H_2SO_4 + KI electrolyte exhibits a stable working voltage of 1.4 V and delivers an energy density of 37.65 Wh kg^{-1} at a power density of 3279 W kg^{-1}. Furthermore, the device retains decent cycling stability over 10 000 cycles.

1 Introduction

Over the past few decades, supercapacitors (SCs) have received a large amount of attention mainly owing to their higher energy density compared to conventional capacitors and superior power density compared to batteries.[1,2] Besides, SC exhibits other attributes, including long cycling stability, a wider working temperature, and impressive safety, which make them an energy storage device of choice for various applications.[3–5] Based on the charge storage mechanism, SC are typically classified into electric double layer capacitors (EDLCs), pseudocapacitors and hybrid capacitors.[6,7] EDLCs, which are based on carbonaceous materials, store charge through the accumulation of charge at the electrode/electrolyte interfaces *via* a non-faradaic reaction, whereas pseudocapacitors store charges through the charge transfer process between the electrode and electrolyte *via* a fast faradaic reaction.[8,9] Pseudocapacitors are commonly fabricated using transition metals and conducting polymers. On the other hand, hybrid SCs exhibit the charge storage mechanism of both EDLCs and pseudocapacitors. Although pseudocapacitors deliver higher specific capacitance and thus superior energy density, the inferior rate performance and limited cycling stability remain major drawbacks.[10,11] Conversely, EDLCs that exhibit excellent rate capability and almost-infinite cycle life suffer from low energy density, which is mainly attributed to their surface-dependent charge storage.[12,13] It is worth noting that the energy density of SC is related to the capacitance of the electrode materials and the stable working voltage of the electrolyte. Although various attempts have been made to tune the properties of the electrode materials, the approach to improving the stable working voltage of aqueous electrolyte-based SCs is limited.[14] Of special attention, redox additive electrolyte, which contains species capable of undergoing redox reactions, has emerged as a promising electrolyte for enhancing the supercapacitive performance of carbonaceous SCs.[15,16] This class of electrolyte is typically prepared by adding a small amount of redox-active species, such as ferricyanide, hydroquinone, or transition metal ions, to the

---

Institute for Nanotechnology and Water Sustainability, College of Science, Engineering and Technology, University of South Africa, Florida Science Campus, 1710, South Africa. E-mail: idrisbm@unisa.ac.za

conventional electrolyte.[17,18] Besides reducing the solution resistance of the conventional electrolyte, the presence of redox species enhances the charge transfer rate by lowering the charge transfer resistance. Furthermore, the rapid and reversible shuttling of redox pairs between the electrode and the electrolyte interfaces results in pseudocapacitance, which enhances the overall performance of SC.[19,20] Indeed, various researchers have reported enhancements in the supercapacitive performance of several carbon-based materials, including reduced graphene oxides,[12,15] carbon fibres,[16] functionalized carbon nanotubes,[17] and honeycomb-like carbon,[17] as well as porous carbon,[18] using various redox additive couples. Beyond supercapacitors, KI and other iodide-based redox mediators have been widely employed in diverse electrochemical systems, including Li–O_2 batteries and aqueous metal-ion batteries.[21,22] For instance, Lei *et al.*,[22] reported the use of KI as a mediator to facilitate the dissolution of MnO_2 and recover 'lost' capacity from exfoliated MnO_2, thereby improving cycling stability. The zinc–manganese battery exhibits improved cycling stability over 400 cycles at 2.5 mA h cm^{-2} in the presence of iodide mediator. It is worth noting that the KI system exhibits higher intrinsic reaction kinetics and stronger pseudocapacitive enhancement than other redox additives.[23] Nonetheless, it is susceptible to diffusion-related limitations at elevated operating rates.[20]

Mesoporous graphitic carbon nitride (CR-gCN), exhibiting high nitrogen content, superb thermal and mechanical stability, and excellent textural properties, among others, has emerged as a promising electrode material for SCs.[1,24,25] Besides the utilisation of pristine graphitic carbon as a standalone electrode material for SC, various composites containing metal oxides and conducting polymers were reported. For instance, Jiang *et al.*[26] reported a specific capacitance of 668 F g^{-1} at a current density of 2 A g^{-1} for cobalt sulfide/GCN nanosheet hybrid composite in 3 M KOH.[17] Chen *et al.*[27] reported a specific capacitance of 264 F g^{-1} at a current density of 0.4 A g^{-1} for an asymmetric capacitor constructed using three-dimensional graphitic carbon nitride functionalized graphene composites. Nanostructured needles like $NiCo_2O_4$ on GCN exhibited a capacitance of 253 F g^{-1} at a current density of 2 A g^{-1} in 6 M KOH.[28] While previous studies have investigated redox-additive electrolytes in carbon-based systems, as highlighted above, the performance of the CR-gCN electrode in redox additive electrolytes has not yet been reported. Furthermore, understanding the charge transfer kinetics at electrode/electrolyte interfaces provides invaluable information, which enables the rational design of various interfaces between the electrode and the electrolyte, thereby achieving optimal performance.

In this work, the capacitance properties of CR-gCN in H_2SO_4 and H_2SO_4-based redox electrolytes containing $K_3Fe(CN)_6$ and KI are reported. The cyclic voltammetry technique is employed to understand the mechanism and kinetics of charge transfer in H_2SO_4-based redox electrolytes.

2 Experimental

2.1 Materials and methods

All chemicals used in the present study were of analytical grade and used as received from Sigma-Aldrich.

2.2 Synthesis of CR-gCN

In a typical synthesis, 0.3 g of carboxymethylcellulose (CMC) with an average molecular weight of ≈700 000 was dissolved in 1 : 2 ethanol : water mixture under constant stirring. To this mixture, 1.6 g of melamine and 5 g of 50% glutaraldehyde were added, and the stirring was maintained for 10 minutes. Subsequently, the pre-condensation of melamine and glutaraldehyde was initiated by raising the reaction temperature to 70 ° C for 4 hours. The obtained CMC/melamine/glutaraldehyde pre-condensed composite was dried at 80 °C followed by crushing into a fine powder. The fine powder thus obtained was transferred into a crucible with a lid, covered with aluminium foil, and finally carbonised at 600 °C for 4 hours. The product obtained was washed with 1.0 M HCl, rinsed with distilled water and finally with ethanol.

2.3 Preparation of redox-additive electrolyte

In a typical synthesis, either 0.823 g of potassium ferricyanide ($K_3Fe(CN)_6$) or 0.415 g of potassium iodide (KI) was added to a 50 mL capacity volumetric flask. Subsequently, 1 M H_2SO_4 solution was added to the above flask and made up to the 50 mL mark to obtain either 1 M H_2SO_4 + 0.05 M $K_3Fe(CN)_6$ or 1 M H_2SO_4 + 0.05 M KI electrolyte. Although (K_3 [$Fe(CN)_6$]) is generally stable in neutral and alkaline solutions, it may release hydrogen cyanide (HCN) under strongly acidic conditions or upon heating; therefore, acidic ferricyanide solutions must be prepared and handled with care.

2.4 Physiochemical characterisation

The Powdered X-ray Diffraction (PXRD) pattern of CR-gCN was recorded using a Rigaku Smart Lab X-ray diffractometer equipped with Cu Ka as the radiation source. The bulk chemical composition of the CR-gCN sample was recorded using a 400 series Spotlight PerkinElmer Fourier transform infrared (FTIR) spectrophotometer using the KBr pellet technique. The microstructures in CR-gCN were studied using FEI Teiknnai F30-S TWIN high-resolution transmission electron microscope (HR-TEM) and ZEISS field-emission scanning electron microscope (FE-SEM). The surface area analysis of the as-prepared sample was investigated using a Micromeritics TriStar II 3020 3.02 surface area analyser. Before the sorption study, the sample was degassed at 150 °C for 4 hours under vacuum and nitrogen was used as the adsorptive gas.

2.5 Electrochemical characterisation

The capacitance properties of CR-gCN were firstly evaluated under a three-electrode system using CR-gCN coated onto a stainless steel foil, Pt foil and Ag/AgCl as working, counter and reference electrodes, respectively. The CR-gCN working electrode was fabricated by mixing 80% of the active material, 10% of Super P carbon black and 10% of polyvinylidene difluoride binder. After the above mixture was manually ground, a few drops of *N*-methylpyrrolidone solvent were added to form a slurry, which was then coated onto a pretreated stainless steel foil and finally dried overnight at 80 °C. The capacitance properties of CR-gCN were recorded in both pristine (1 H_2SO_4) and redox-additive electrolytes (1 M H_2SO_4 + 0.05 M $K_3Fe(CN)_6$ and 1 M H_2SO_4 + 0.05 M KI) using a BioLogic VMP-3e Multichannel Potentiostat.

3 Results and discussion

3.1 Physicochemical characterisation of CR-gCN

The powder X-ray diffraction is utilised to study structural characteristics of the CR-gCN, and the result is depicted in Fig. 1a. The PXRD peaks witnessed at $2\theta \approx 13.57°$, 26.24° and 43.01° (101), corresponding to the graphite-like stacked structures in g-CN and amorphous carbon correspond to the (100), (002) and (101) planes respectively, found in GCN.[24,29,30] While the (100) reflections arise from in-plane structural packing of tri-*s*-triazine units, the (002) peak corresponds to the interlayer stacking found in conjugated aromatic systems.[31,32] The broadness of the (002) peak indicates poor crystallinity in CR-gCN domains. Besides, the interplanar space of 0.3392 is higher than the value reported for CR-gCN prepared using the hard template method, which could be attributed to the presence of in-plane residual carbon resulting from the decomposition of the precursor and biotemplate during the high-temperature carbonisation.[33–36] The presence of residual carbon domains is expected to facilitate electronic conductivity and enhance charge transfer kinetics during electrochemical processes.[37–39] The functional groups and bonding environment in CR-gCN were investigated using FTIR spectroscopy, and the result is presented in Fig. 1b. The broad absorption at ~3400 cm^{-1} is assigned to N–H and/or O–H stretching found in amine groups and/or surface hydroxyls.[40] The weak peak seen at around 2090 cm^{-1} corresponds to C=O, whereas the stretching vibrations of C=N and C–N heterocycles were observed at a wavenumber of ~1630 and 1240 cm^{-1}, respectively.[41,42] The

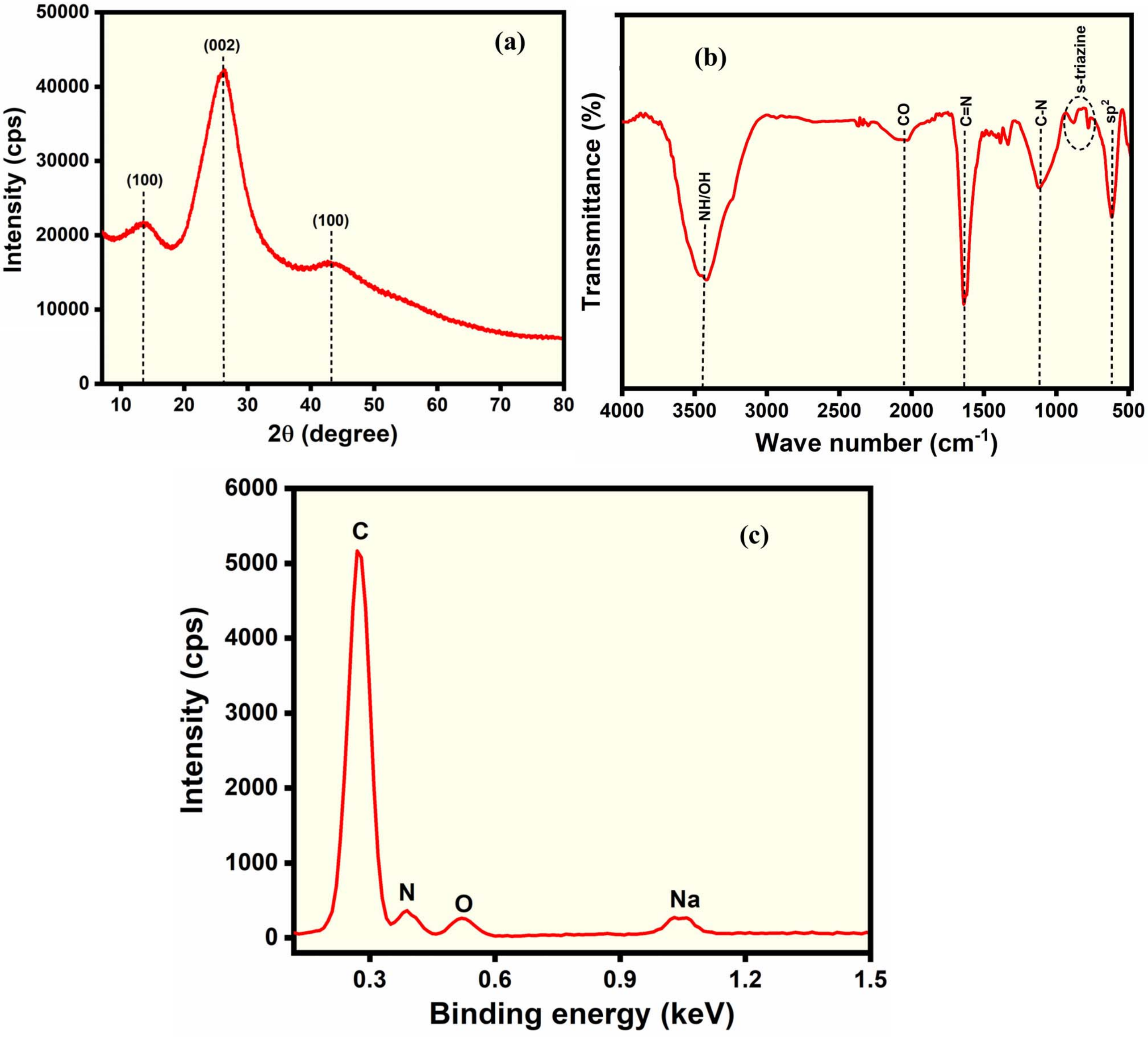

Fig. 1 (a) PXRD pattern, (b) FTIR and (c) EDX spectra of CR-gCN.

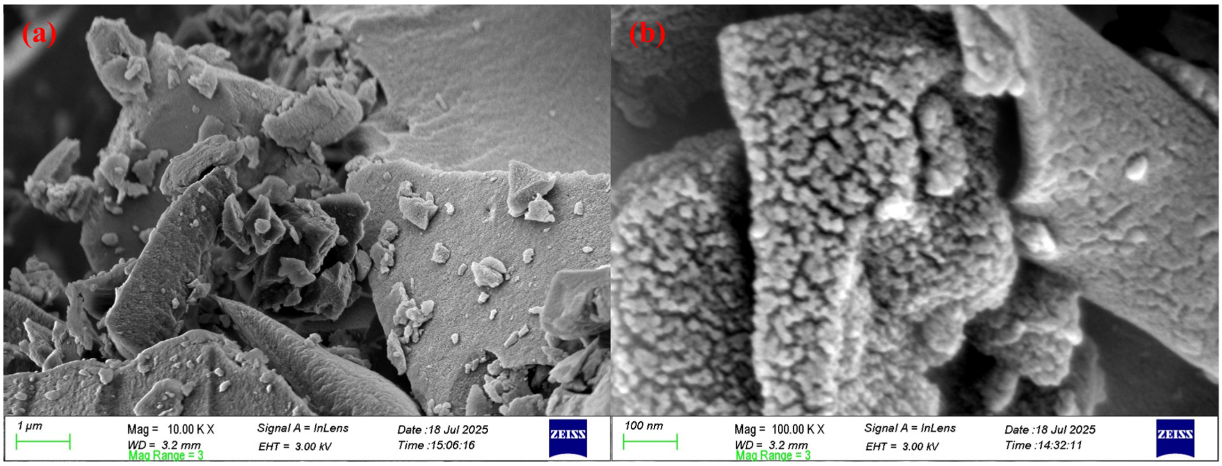

Fig. 2 (a) Low and (b) high magnification FE-SEM images of CR-gCN.

band at ∼810 cm^{-1} corresponds to the breathing mode of *s*-triazine units found in the polymeric heptazine framework. The peak observed at around 606 cm^{-1} is attributed to the presence of sp^2 domains in amorphous carbon, further suggesting the presence of amorphous carbon domains.[43] The energy dispersive X-ray (EDX) spectrum presented in Fig. 1c reveals the presence of peaks corresponding to carbon, nitrogen and oxygen, with a relative atomic weight of 63.70, 23.90 and 10.90% respectively. The minor peak, which corresponds to sodium with a relative atomic weight of 1.5% could have arisen from the sodium CMC template used during the synthesis. The higher relative atomic weight of carbon further confirms the incorporation of residual carbon originating from the thermal decomposition of precursors and template.[12,44]

The microstructures in CR-gCN were studied using FE-SEM and TEM. As seen in Fig. 2a, the SEM image of CR-gCN reveals the presence of micron-scale platelet-like structures stacked together to form a loosely packed, three-dimensional network. It can be observed that the surface of the FE-SEM image of CR-gCN at high magnification is composed of rough surfaces, implying the presence of pores (Fig. 2b). The observed surface roughness in the FE-SEM image of CR-gCN is believed to originate from the thermal decomposition of the pre-mounted biotemplate during carbonisation, which is expected to facilitate the surface accessibility of ions and improve mass transport diffusion.

The low-resolution TEM image of CR-gCN reveals a stacked and partially transparent flake-like nanostructure (Fig. 3a). The inability of the electron beam to transmit through the stacked

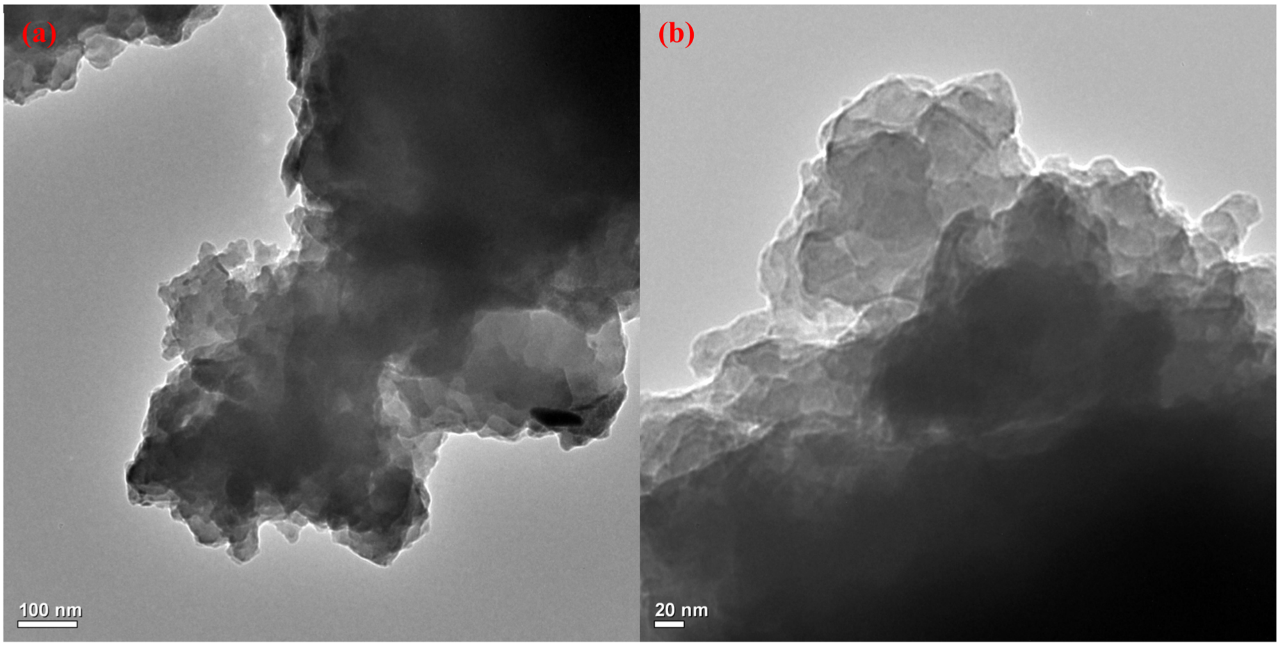

Fig. 3 (a) Low and (b) HR-TEM images of CR-gCN.

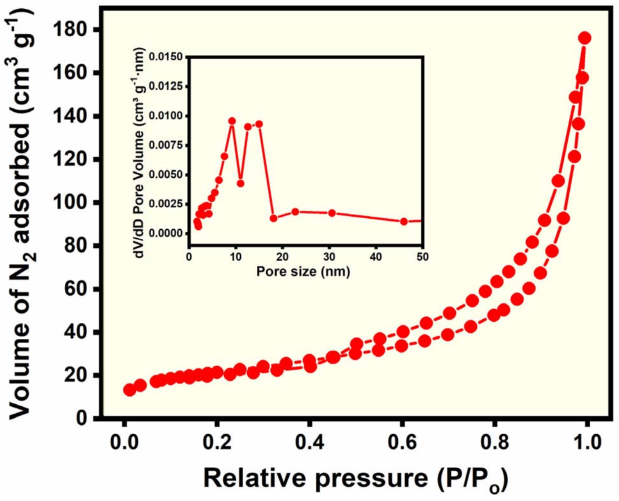

Fig. 4 Nitrogen adsorption–desorption isotherms of CR-gCN with BJH pore size distribution as an inset.

layers of CR-gCN resulted in the presence of dark spots in the low-resolution TEM image. The observed improvement in transparency along the edges of the high-resolution TEM image of CR-gCN (Fig. 3b) is attributed to the reduced degree of stacking and partial exfoliation at the sheet edges.

The textural properties of CR-gCN were analysed using nitrogen adsorption–desorption isotherms, and the results are presented in Fig. 4. The nitrogen isotherm of CR-gCN exhibits a type IV hysteresis loop in the relative pressure range of 0.49–0.98 (Fig. 4), a typical property of mesoporous material.[35] Furthermore, the presence of H_3 loops suggests that the mesopore originated from the aggregation of plate-like particles.[45] The multi-point Brunauer–Emmett–Teller (BET) surface area is 85.48 $m^2\ g^{-1}$, and the pore volume is 0.275 $cm^3\ g^{-1}$. The surface area and pore volume obtained in the present study are significantly higher than those obtained for GCN prepared by direct thermal carbonisation of the precursor, a clear indication of the role of the biotemplate in enhancing the textural properties of GCN.[46–48] As witnessed in Fig. 4a (in set), the Barrett–

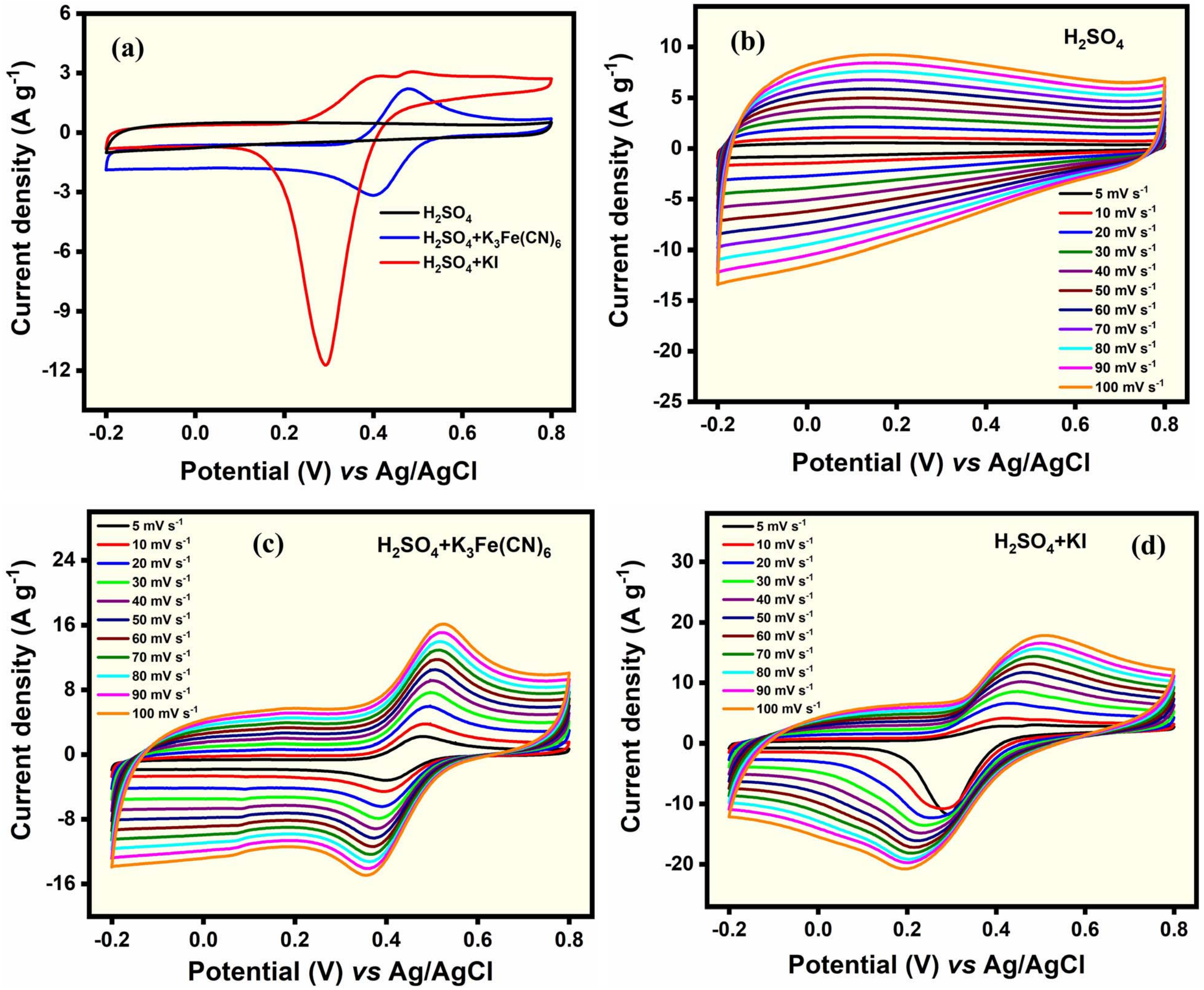

Fig. 5 (a) Combined CVs of the CR-gCN electrode in pristine and redox-additive electrolytes recorded at a scan rate of 5 mV s^{-1}. CVs recorded at various scan rate ranges from 5 to 100 mV s^{-1} in (b) 1 M H_2SO_4, (c) H_2SO_4 + $K_3Fe(CN)_6$ and (d) H_2SO_4 + KI electrolytes.

Joyner–Halenda (BJH) pore size distribution indicated that the average pore size is centred around 7.7 nm.

3.2 Electrochemical characterisation of C-gCN electrode under three configurations

The electrochemical performance of CR-gCN electrode is evaluated in both pristine and redox-active electrolytes using cyclic voltammetry (CV). As shown in Fig. 5a, the CV profile of CR-gCN in 1 M H_2SO_4 exhibits a pseudo-rectangular shape, characteristic of electric double-layer capacitive and surface faradaic redox behaviour.[49,50] While the double-layer capacitance is ascribed to the adsorption/desorption of ions on/from the surface of the electrode materials, the faradaic reactions of nitrogen and oxygen functionalities contribute to the pseudocapacitance.[34] Upon the introduction of either $K_3Fe(CN)_6$ or KI into the pristine electrolyte, distinct redox peaks were witnessed, which correspond to a reversible reaction involving electron transfer in the redox systems. The redox shuttling operating in the redox additive-based electrolytes results in the enhancement in the area under the CV curve of the CR-gCN electrode in both 1 M H_2SO_4 + 0.05 M $K_3Fe(CN)_6$ (H_2SO_4 + $K_3Fe(CN)_6$), and 1 M H_2SO_4 + 0.05 M KI (H_2SO_4 + KI) electrolyte. Furthermore, it can be observed that the area under the CV profile of the H_2SO_4 + KI system is significantly higher than that of H_2SO_4 + $K_3Fe(CN)_6$ system, an indication that CR-gCN stores a higher number of charges in the H_2SO_4 + KI electrolyte. It is noteworthy that the KI-containing electrolyte exhibits asymmetric anodic/cathodic currents, which is characteristic of iodide–polyiodide electrolytes.[51] This behaviour arises from the tendency of triiodide species to interact strongly with carbonaceous surfaces, and their partial retention, which can lead to disproportionate current densities during forward and reverse scans.[52] The redox reaction operating in H_2SO_4 + $K_3Fe(CN)_6$ and H_2SO_4 + KI is presented in eqn (1)–(4), respectively.[51,53]

$$[\mathrm{Fe(CN)_6}]^{4-} \leftrightarrow [\mathrm{Fe(CN)_6}]^{3-} + \mathrm{e}^- \quad E^0 = \approx +0.16\ \mathrm{V}\ vs.\ \mathrm{Ag/AgCl} \tag{1}$$

$$3\mathrm{I}^- \leftrightarrow \mathrm{I_3}^- + 2\mathrm{e}^- \quad E^0 = \approx +0.339\ \mathrm{V}\ vs.\ \mathrm{Ag/AgCl} \tag{2}$$

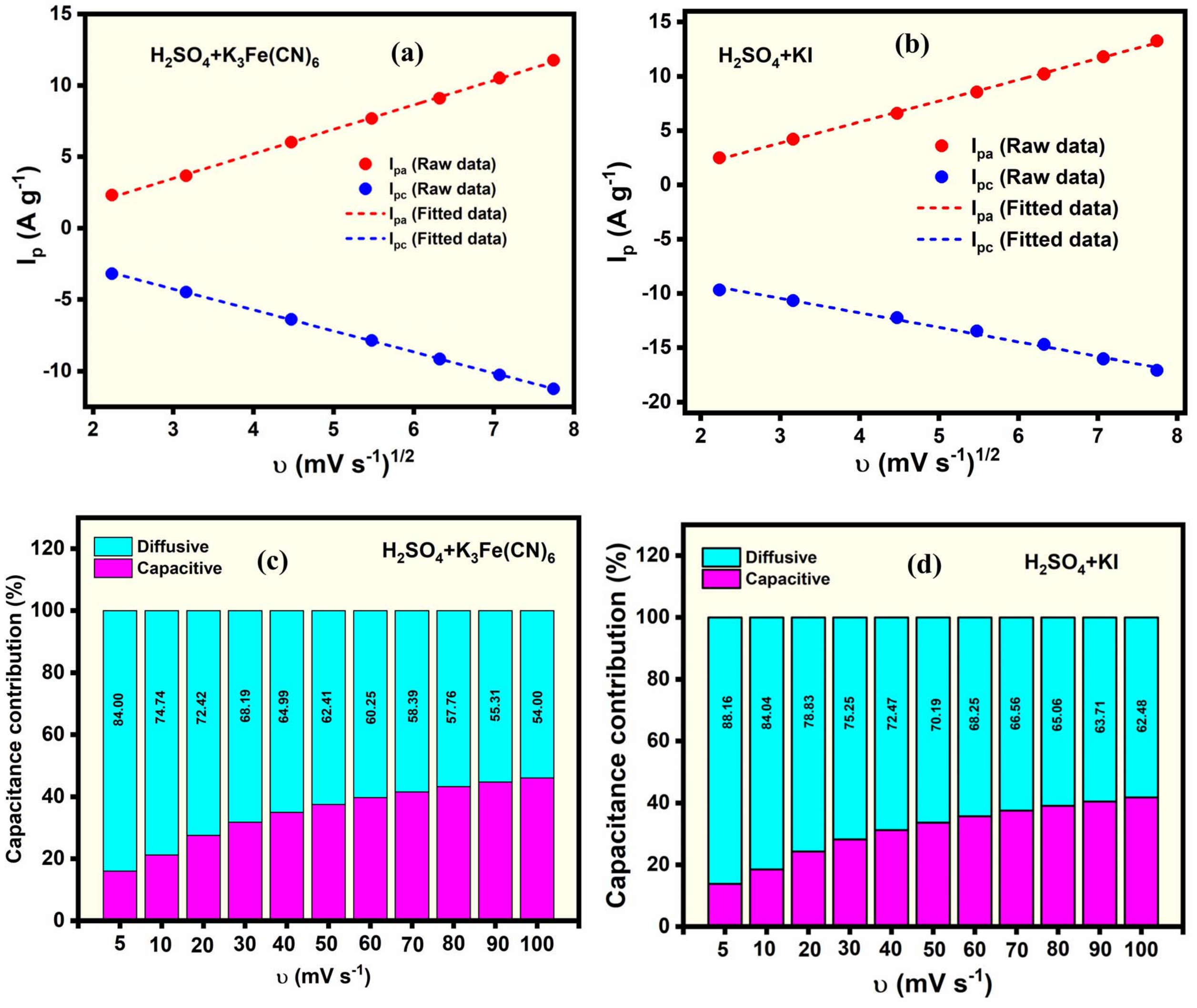

Fig. 6 Randles–Sevcik plot (i_p *vs.* $\nu^{1/2}$) and percentage capacitance contributions of CR-gCN in (a and c) H_2SO_4 + $K_3Fe(CN)_6$ and (b and d) H_2SO_4 + KI electrolytes.

Table 1 Kinetic parameters obtained from redox-additive electrolytes

Electrolyte	D ($\mathrm{cm^2\ s^{-1}}$)	k^0_{eff} ($\mathrm{cm\ s^{-1}}$)	b
$H_2SO_4 + K_3Fe(CN)_6$	8.43×10^{-5}	0.284	0.6460
H_2SO_4 + KI	4.0×10^{-4}	0.453	0.6399

$$2I^- \leftrightarrow I_2 + 2e^- \quad E^0 = \approx +0.424\ \mathrm{V}\ \mathit{vs.}\ \mathrm{Ag/AgCl} \tag{3}$$

$$2I_3^- \leftrightarrow 3I_2 + 2e^- \quad E^0 = \approx +0.592\ \mathrm{V}\ \mathit{vs.}\ \mathrm{Ag/AgCl} \tag{4}$$

The higher charge storage capability of CR-gCN in H_2SO_4 + KI compared to $H_2SO_4 + K_3Fe(CN)_6$ is attributed to the ability of KI to undergo fast transformation into the I^-/I_3^- redox couple.[18] The formed iodide readily forms polyiodide species that can be weakly adsorbed to the CR-gCN surface, enabling rapid, reversible electron transfer at the electrode interface. Fig. 5b–d present the scan rate-dependent CV responses of CR-gCN in pristine, $H_2SO_4 + K_3Fe(CN)_6$ and H_2SO_4 + KI systems, respectively. Evidently, the CV curves in pristine electrolyte maintain their quasi-rectangular shape even at a high scan rate of 100 mV s^{-1}, demonstrating good reversibility and capacitive behaviour. In contrast, both $K_3Fe(CN)_6$ and KI electrolytes display progressive shifts in the anodic and cathodic peak potentials with increasing scan rate, a characteristic of quasi-reversible electron-transfer kinetics. In general, driving interfacial charge transfer at higher scan rates leads to the formation of thinner diffusion layers, which, in turn, introduce mass-transport limitations that require larger overpotentials to drive the reaction.[54,55]

To understand the mechanism of charge storage and mass-transport limitations in the redox additive electrolytes, a Randles–Sevcik equation is utilised (eqn (5)).

$$I_p = 2.69 \times 10^5 \times A \times C \times n^{\frac{3}{2}} \times D^{1/2} \times \nu^{1/2} \tag{5}$$

where I_p is the peak current density, A is the area of the electrode, D is the diffusion coefficient, n is the number of electron transfers, C is the concentration of the electroactive species and ν is the scan rate. As presented in Fig. 6a and b, the linear variation of anodic and cathodic I_p with the square root of scan

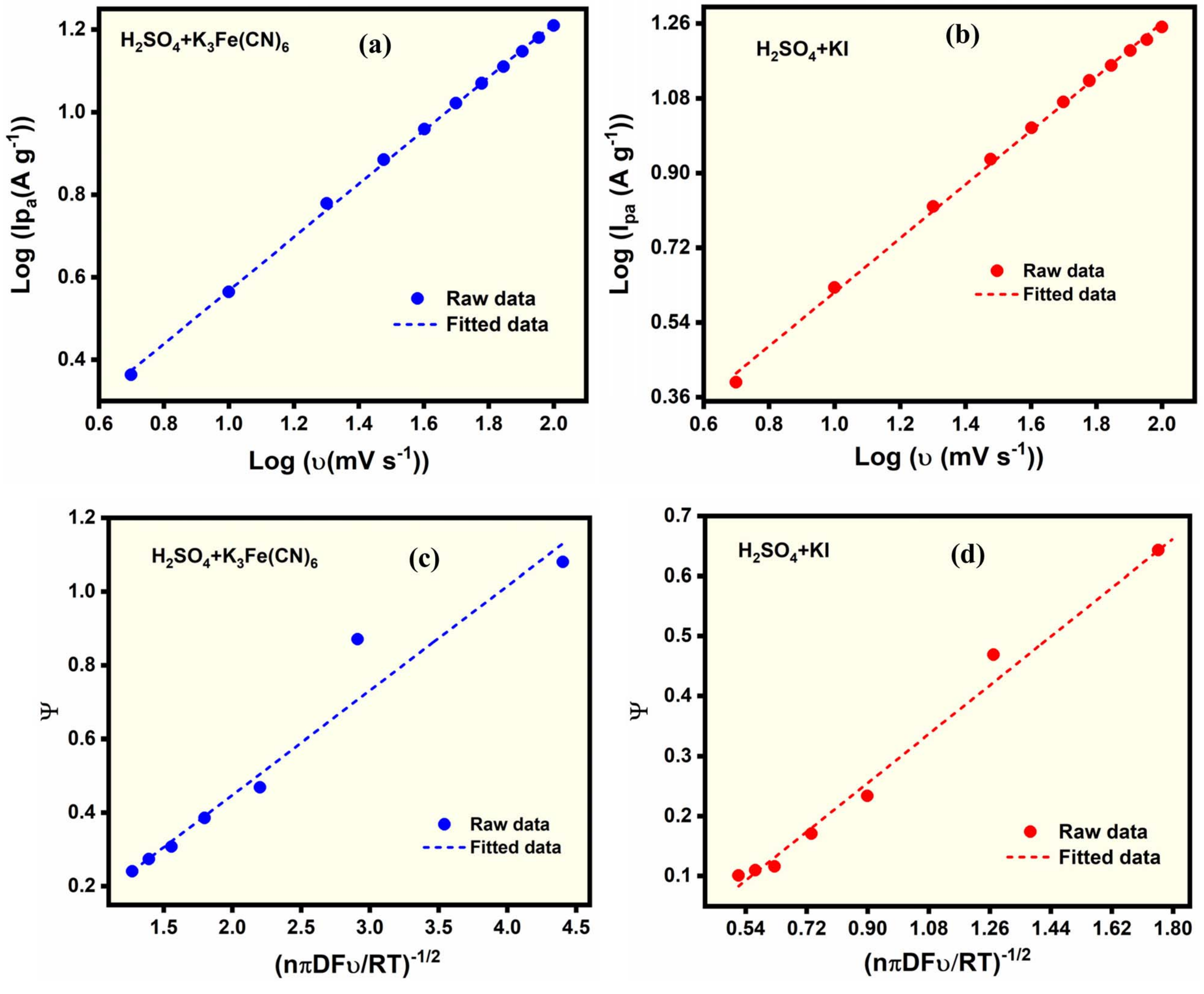

Fig. 7 Plot of log i_p *vs.* log $\nu^{1/2}$ and Ψ obtained using Nicholson's method *vs.* $(n\pi DF\nu/RT)^{-1/2}$ in (a and c) $H_2SO_4 + K_3Fe(CN)_6$ and (b and d) H_2SO_4 + KI electrolytes.

rate ($\nu^{1/2}$) in both electrolytes suggests that charge storage in both redox additive electrolytes is diffusion-controlled. Furthermore, it can be inferred from Table 1 that the diffusion coefficient of 4.0×10^{-4} cm^2 s^{-1} for the KI electrolyte is ~4.7 times higher than that of $K_3Fe(CN)_6$ electrolyte, suggesting faster, higher conversion of iodide ions into triiodide ions and their subsequent transport from the bulk to the electrode interface. The lower diffusion coefficient of the $K_3Fe(CN)_6$ electrolyte can be attributed to the larger ionic size of the solvated $[Fe(CN)_6]^{3-}$, leading to slower translational diffusion.[56] To further understand the charge storage mechanisms and quantify the capacitance contribution of CR-gCN in redox additive electrolyte, the Dunn method is employed.[57]

$$i(V) = i_{\text{cap}} + i_{\text{diff}} = k_1\nu + k_2\nu^{1/2} \quad (6)$$

where V is the potential, k_1 and k_2 are constants, and $k_1\nu$ and $k_2\nu^{1/2}$ are the current contributions from the surface capacitive and the diffusion-controlled processes, respectively. k_1 and k_2 are obtained from the slope and intercept of plot of $i(V)/\nu^{1/2}$ *vs.* $\nu^{1/2}$. Although the diffusion-controlled mechanism dominates the capacitance contribution in both electrolytes at lower scan rates (Fig. 6c and d), the H_2SO_4 + KI electrolyte exhibits a higher diffusive contribution at higher scan rates, indicating a rapid charge storage kinetics.

To evaluate the charge storage mechanism of CR-gCN electrode in redox additive electrolytes further, the power law, which expresses the relationship between I_p *vs.* ν is used.[58]

$$i_p = a\nu^b \quad (7)$$

where i_p is a peak current density, ν represents the scan rate, and a and b are constants. In principle, if $b = 0.5$, it corresponds to the diffusion-controlled charge storage mechanism, whereas if $b = 1$, it corresponds to the surface-dominated capacitive process. Conversely, ab value in the range of 0.5 to 1 is

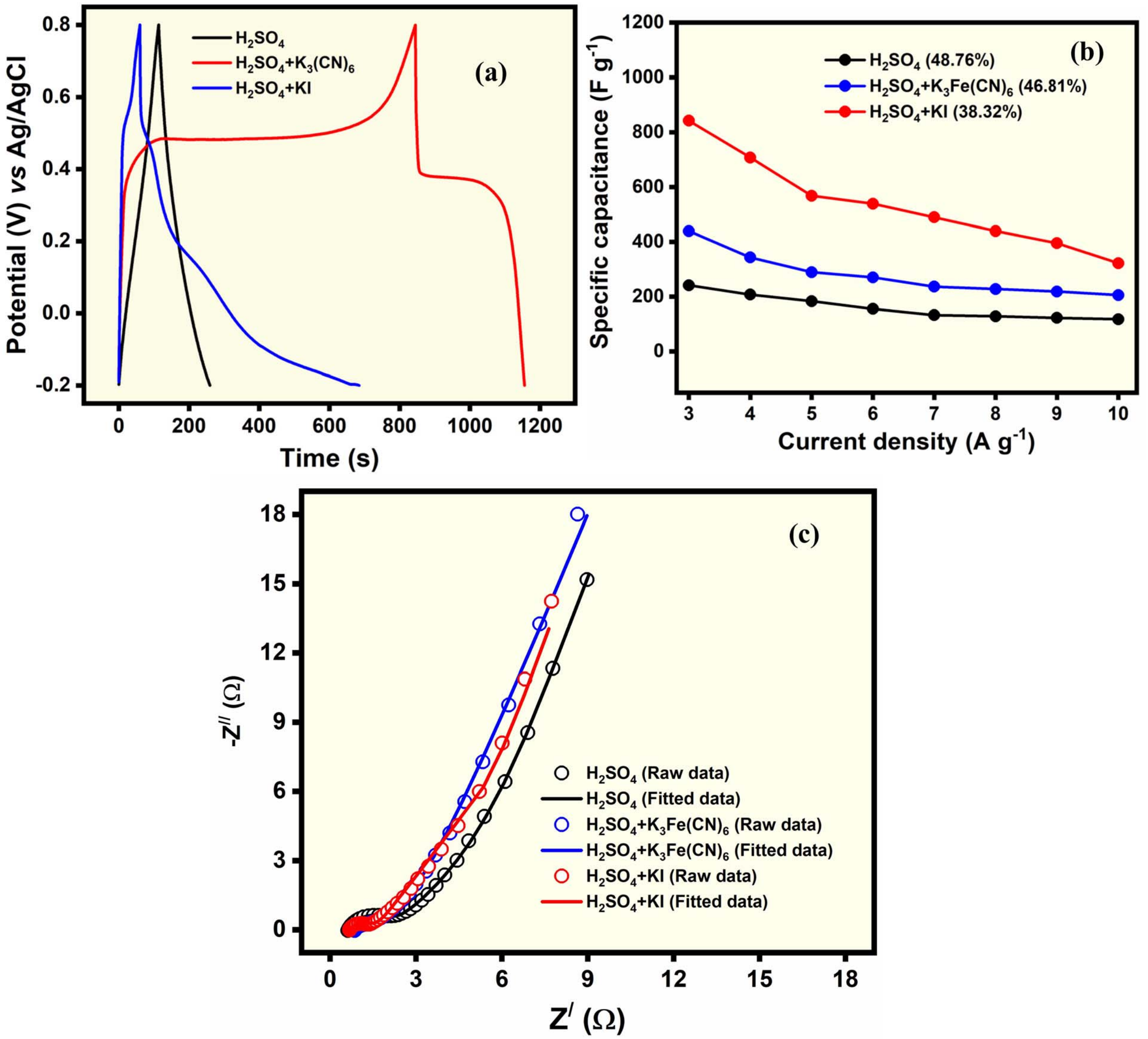

Fig. 8 (a) GCD curves recorded at a current density of 3 A g^{-1}, (b) rate performance and (c) Nyquist plot of CR-gCN in pristine and redox-additives based electrolytes.

considered a mixed process. The estimated b values for the CR-gCN in $H_2SO_4 + K_3Fe(CN)_6$ and H_2SO_4 + KI obtained from the plot of log (i_p) *vs.* log (v) (Fig. 7 and Table 1) are 0.6460 and 0.6399. The slightly lower b value in H_2SO_4 + KI suggests a higher diffusion-controlled process, which is consistent with higher diffusive contributions at higher scan rate.

The charge transfer kinetics of CR-gCN in redox additive electrolytes are investigated using modified Nicholson's method.[59,60] The heterogeneous charge transfer constant (k^0_{eff}) values were calculated using eqn (8).

$$k^0_{\text{eff}} = \frac{\pi DnFv}{RT}\Psi \tag{8}$$

where D is the diffusion coefficient of redox mediator, n is the number of electrons participating in the redox reaction, F is Faraday's constant, v is the scan rate, R is the gas constant, T is the temperature (K), and ψ is the kinetic parameter calculated difference between the anodic and cathodic peaks ($\Delta E_p = |E_{pa} - E_{pc}|$). It can be inferred from Fig. 7c, d and Table 1 that the k^0_{eff} of 0.453 cm s^{-1} for H_2SO_4 + KI is ~1.6 times higher than that of $H_2SO_4 + K_3Fe(CN)_6$, indicating faster interfacial electron transfer in the iodide system. This result is consistent with the charge storage mechanism above.

The specific capacitance in both pristine and redox additive electrolytes is calculated using a galvanostatic charge–discharge (GCD) profile. While the GCD curve of CR-gCN in H_2SO_4 assumed a triangular shape, typical of electric double-layer capacitive behaviour with minor pseudocapacitance, the non-linear discharge profiles in the redox electrolytes indicate faradaic processes (Fig. 8a). The asymmetric GCD profile of CR-gCN in redox additive electrolytes is attributed to the faradaic reaction involving the redox couples. Considering that the redox involves a sequence of electron-transfer and chemical association reactions at different time scales, the potential of the systems changes nonlinearly over time, resulting in a nonlinear GCD profile. It can be observed that the KI system exhibits greater deviation from linearity, which could be attributed to strong adsorption of triiodide species on carbonaceous surfaces.[52] Owing to the capacitance contribution from the faradaic redox reactions, the CR-gCN electrode delivers

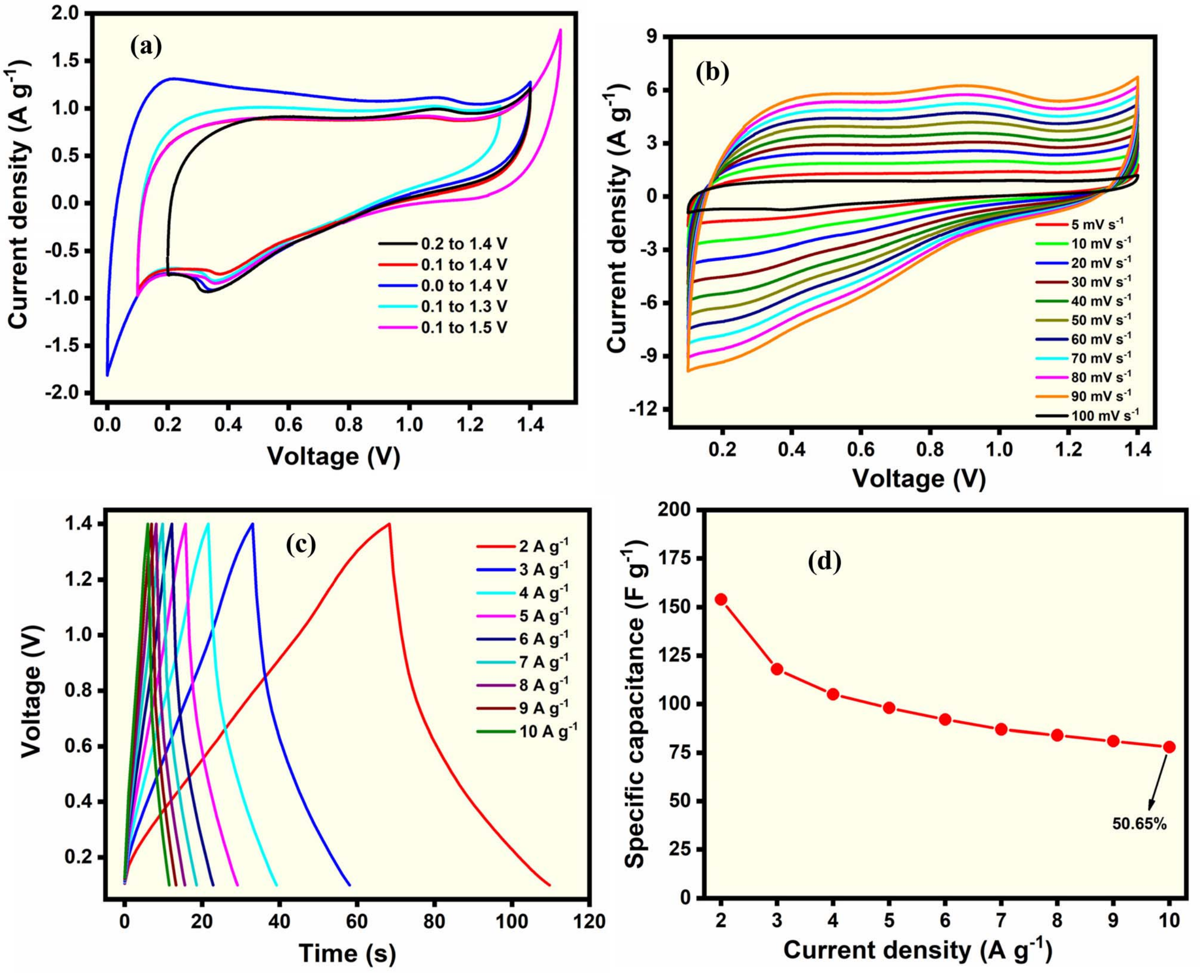

Fig. 9 (a) Voltage optimisation recorded at a scan rate of 5 mV s^{-1}, (b) CVs recorded at various scan rates, (c) GCD curves recorded at various current densities and (d) rate performance of the device in H_2SO_4 + KI electrolyte.

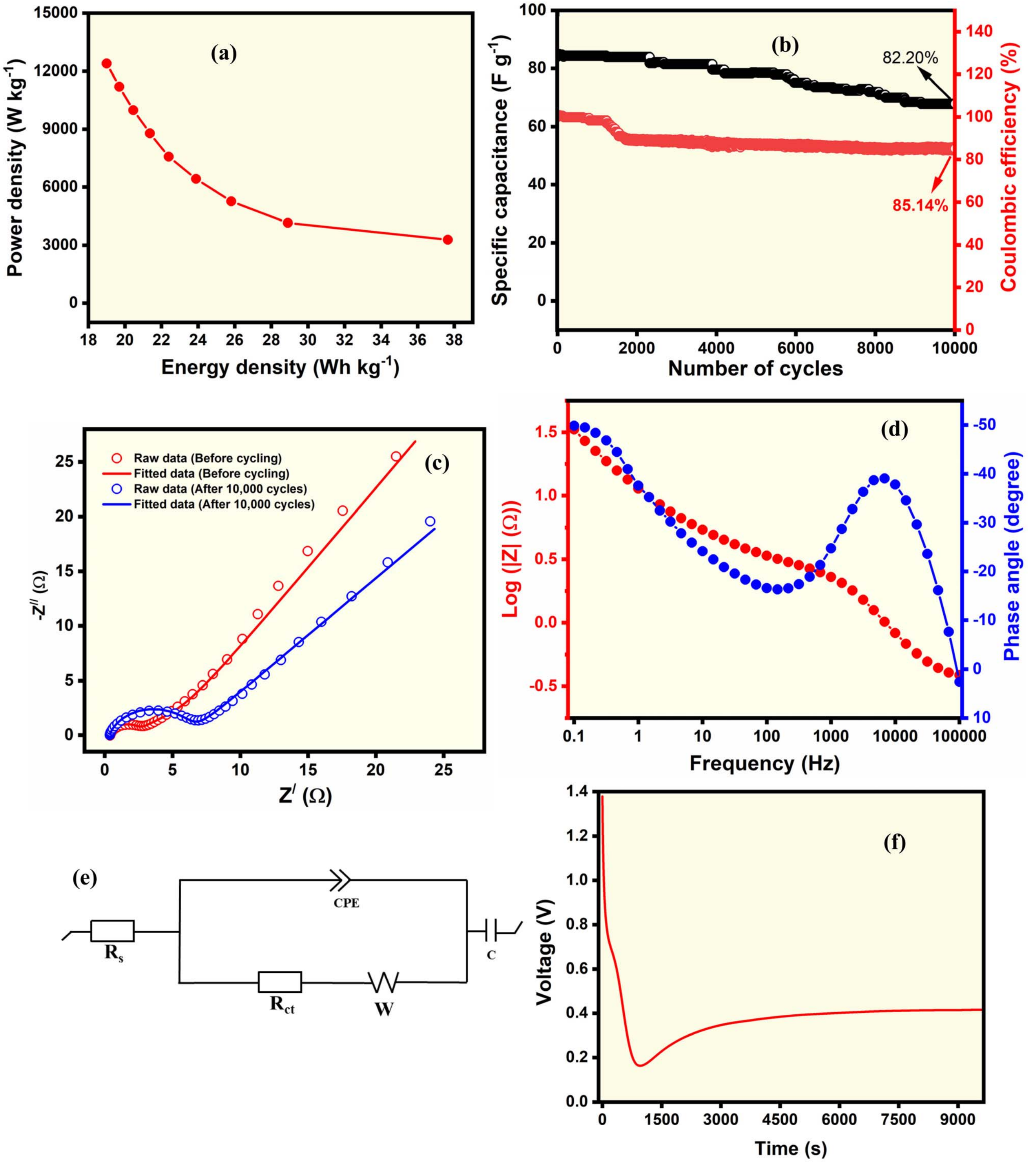

Fig. 10 (a) Ragone plot, (b) cycling stability, (c) Nyquist plot and (d) Bode plot, (e) equivalent circuit used for fitting the EIS spectra and (f) self charge of the device in H_2SO_4 + KI electrolyte.

a specific capacitance of 843 and 440 F g^{-1} at the current density of 3 A g^{-1} in H_2SO_4 + KI and H_2SO_4 + $K_3Fe(CN)_6$ electrolyte, respectively, which is 3.48 and 1.82 times higher than the value obtained in the pristine electrolyte. As shown in Fig. 8b, with increasing current density, all systems exhibit a decline in capacitance due to reduced ion diffusion. Among all the electrolytes, H_2SO_4 + KI exhibits the lowest capacitance retention, which could be attributed to the slower replenishment of redox species near the electrode surface at high discharge rates. In other words, at a higher GCD rate, the electrode rapidly consumes iodide species at the interface, and transport within the porous electrode becomes the rate-limiting step. This is expected to reduce the effective utilisation of the I^-/I_3^- redox couple, leading to the observed drop in capacitance retention.

This behaviour has been reported in iodide-based systems.[23] Electrochemical impedance spectroscopy is employed to understand the influence of the redox additive on the solution and charge resistance, which invariably affects the kinetics of charge transport across the electrode interface. Although there is no significant difference in the values of the solution resistance (Fig. 8c) (R_s, H_2SO_4: 0.65 Ω, H_2SO_4 + $K_3Fe(CN)_6$: 0.701, H_2SO_4 + KI: 0.649 Ω), a marked differences were observed in the charge-transfer resistance (R_{ct}), which followed the order H_2SO_4 (1.782 Ω) > H_2SO_4 + $K_3Fe(CN)_6$ (1.011 Ω) > H_2SO_4 + KI (0.701 Ω). The lower R_{ct} value for H_2SO_4 + KI demonstrates the facile nature of I^-/I_3^- redox couple shuttling, which facilitates rapid interfacial electron transfer. This result agrees well with both k^0_{eff} and diffusion coefficient values.

3.3 Fabrication and evaluation of a symmetrical SC using H_2SO_4 + KI electrolyte

A symmetric SC device was fabricated using CR-gCN and H_2SO_4 + KI electrolyte as the electrode and electrolyte, respectively. The working electrodes were prepared by casting a homogeneous slurry of CR-gCN onto one side of pretreated stainless steel (SS) foil, serving as the current collector. After drying, the two electrodes were assembled using a face-to-face configuration with a Whatman filter paper serving as the separator. Prior to the assembly, both the electrode and the separator were thoroughly soaked in H_2SO_4 + KI electrolyte to ensure complete wetting. During assembly, only the coated side of the CR-gCN electrodes was exposed to the electrolyte, while the uncoated side of the SS foil was insulated using Teflon tape. The electrochemical performance of the fabricated device is evaluated systematically using CV, GCD, cycling stability, and impedance spectroscopy. The specific capacitance (C_{sp}, F g^{-1}), energy density (E, Wh kg^{-1}) and power density (P, W kg^{-1}) of the SC device were calculated using eqn (9)–(11), respectively.[61]

$$C_{sp} = \frac{2i_m \int V\,dt}{V^2\big|_{V_i}^{V_f}} \tag{9}$$

where $i_m = I/m$ is the constant current density in A g^{-1}, m is the mass of the material in the electrode, $\int Vdt$ is the integral current area, where V is the time-dependent voltage, and V_i and V_f are the initial and final voltages.

$$E = \frac{I \int V\,dt}{m} \tag{10}$$

$$P = \frac{E}{t} \times 3600 \tag{11}$$

where I is the current in A, V is the voltage, $\int Vdt$ is the area under the discharge curve, and m is the total mass of the two electrodes and t is the discharge time (s).

Fig. 9a depicts the CV curves recorded at a scan rate of 5 mV s^{-1} with varying upper and lower voltage windows. It can be observed that the device exhibits an electrochemically stable voltage in the range of 0.1 to 1.4 V. Below and beyond these limits, a slight distortion in the CV profile was observed. The hump-like redox peaks observed in the CV of the device are assigned to a reversible iodide redox shuttle. Although water decomposes thermodynamically at 1.23 V, it can be seen that the devices maintain stable operation up to 1.40 V. The presence of the iodide redox couple in the electrolyte participating in the charge storage could have competed with the hydrogen evolution and oxygen evolution reactions, thereby suppressing the water decomposition.[62,63] The CV curves recorded at various scan rates in the range of 5–100 mV s^{-1} are shown in Fig. 9b. It can be seen that the quasi-rectangular shapes of CV are maintained over the range of the scan rate, indicating good reversibility of charge storage processes and rapid charge kinetics at the electrode/electrolyte interface. Furthermore, the monotonic increase in current response with increasing scan rate further suggests a surface and diffusion-controlled mechanism.

Fig. 9c depicts the GCD profile of the device recorded at various current densities ranging from 2 to 10 A g^{-1}. Owing to the combination of both diffusion-controlled and surface-controlled charge storage mechanisms, the GCD profiles of the device display pseudo-symmetric triangular shapes. At a current density of 2 A g^{-1}, the device delivers a specific capacitance of 154 F g^{-1}. On increasing the current density, the specific capacitance decreases (Fig. 9d), which is ascribed to reduced ion diffusion at higher charge/discharge rates. Evidently, the device retained 50.65% of its initial specific capacitance when the current density increased from 1 to 10 A g^{-1}, demonstrating decent rate capability. The calculated energy and power densities of the device are presented as a Ragone plot (Fig. 10a). It can be inferred that the device delivers an energy density of 37.65 Wh kg^{-1} at a power density of 3279 W kg^{-1}. When the high power density is increased to 9,980 W kg^{-1}, the device still delivers an energy density above 24.46 Wh kg^{-1}. Cycling stability is a crucial parameter for evaluating the durability of the electrolyte in the device. As shown in Fig. 10b, although the device exhibits decent cycling stability over 10 000 cycles (82.20%), it exhibits a coulombic efficiency which is substantially below unity (85.1%). To understand the reason for the loss in specific capacitance when the device is subjected to continuous charge/discharge cycles, electrochemical impedance spectroscopy (EIS) is used. The equivalent circuit used for fitting the EIS spectra is presented in Fig. 10e. The Nyquist plots presented in Fig. 10c reveal that the R_s decreases marginally after 10 000 cycles, which could be attributed to the improved wettability of the electrode by the electrolyte. On the other hand, the R_{ct} of 2.764 Ω before cycling stability increased to 6.572 Ω, which represents more than a two-fold increment. Therefore, it's reasonable to attribute the loss in the specific capacitance to the increase in the R_{ct} caused by surface passivation. Furthermore, the increment in the value of the phase angle after the cycling stability suggests that the capacitance contribution from the diffusion-controlled process diminishes over time. Additionally, the increase in the magnitude of $|Z|$ after cycling stability further suggest the decrease in capacitance contribution from the redox process, which might be due to pore blockage and surface passivation.[64]

The self-discharge behaviour of the device is investigated by using the open-circuit voltage (OCV) technique. As shown in

Fig. 10f, the device shows a rapid initial drop followed by a slower decay/relaxation toward a lower quasi-steady potential. In general, the rapid self-discharge of the device in the KI-based redox electrolytes is attributed to the migration/diffusion of the electroactive species.[65] Therefore, both the sub-unity coulombic efficiency and the two-stage OCV decay could be attributed to the diffusion of polyiodide species formed during oxidation away from the charged electrode and their subsequent reduction at the opposite electrode or current collector, producing a continuous internal leakage.[65]

4 Conclusion

In summary, the enhancement in the capacitance properties of CR-gCN using a redox additive electrolyte, as well as insights into the mechanism and charge-transfer kinetics at the electrode/electrolyte interfaces, are investigated. The electrochemical studies revealed that the CR-gCN electrode delivers a specific capacitance of 843 F g^{-1} at 3 A g^{-1} in a KI-based electrolyte, which is ~3.5-fold higher than in the pristine H_2SO_4 electrolyte, whereas the charge storage mechanism studies indicated that a diffusion-controlled process dominates the capacitance contribution in the redox additive electrolyte. The charge transfer kinetics of CR-gCN in redox additive electrolyte reveals that H_2SO_4 + KI electrolyte exhibits a heterogeneous charge transfer constant (k^0_{eff}) of 0.453 cm s^{-1} which is ~1.6 times higher than that of H_2SO_4 + $K_3Fe(CN)_6$, indicating faster interfacial electron transfer in the iodide system. A symmetric device fabricated with H_2SO_4 + KI sustained a stable operating voltage of 1.4 V, beyond the theoretical limit of water and energy density of 37.65 Wh kg^{-1} at a power density of 3279 W kg^{-1}. Furthermore, the device retained decent cycling stability over 10 000 cycles.

Author contributions

Mustapha Balarabe Idris: conceptualization, data curation, formal analysis, investigation, validation, writing and editing. Bhekie B. Mamba: editing, funding acquisition, project administration, Fuku Xolile: editing, funding acquisition, project administration, resources, supervision, visualization, writing – review & editing.

Conflicts of interest

The authors declare that they have no known competing financial interests or personal relationships that could have appeared to influence the work reported in this paper.

Data availability

Data will be made available on request.

Acknowledgements

The authors would like to express their gratitude to the University of South Africa, the Institute for Nanotechnology and Water Sustainability (iNanoWS), College of Science, Engineering, and Technology for funding and research facilities. During the preparation of this work, the author(s) used Grammarly software for spelling, grammar, and punctuation checks. After using this tool, the author(s) reviewed and edited the content as needed and take(s) full responsibility for the content of the published article.

References

1 M. B. Idris, Z. Musa Mohammed, S. Nuhu, H. Aliyu, H. Abba, B. B. Mamba, D. Sappani and F. Xolile, Recent Advances in Mesoporous Carbon Nitride-Based Materials for Electrochemical Energy Storage and Conversion and Gas Storage, *ACS Omega*, 2025, **10**(18), 18184–18212.
2 M. B. Idris, S. Nuhu, Z. M. Mohammed, H. Aliyu, H. Abba, F. Xolile and S. Devaraj, Progress in Metal-Organic Frameworks and Their Carbon-Based Composites for Supercapacitor, *J. Energy Storage*, 2024, **93**, 112322.
3 P. J. Hall, M. Mirzaeian, S. I. Fletcher, F. B. Sillars, A. J. Rennie, G. O. Shitta-Bey, G. Wilson, A. Cruden and R. Carter, Energy Storage in Electrochemical Capacitors: Designing Functional Materials to Improve Performance, *Energy Environ. Sci.*, 2010, **3**(9), 1238–1251.
4 D. S. Su and R. Schlögl, Nanostructured Carbon and Carbon Nanocomposites for Electrochemical Energy Storage Applications, *ChemSusChem*, 2010, **3**(2), 136–168.
5 Y. A. Kumar, S. Vignesh, T. Ramachandran, K. D. Kumar, A. G. Al-Sehemi, M. Moniruzzaman and T. H. Oh, Solidifying the Future: Metal-Organic Frameworks in Zinc Battery Development, *J. Energy Storage*, 2024, **97**, 112826.
6 P. V. Vardhan, M. B. Idris, H. Y. Liu, S. R. Sivakkumar, P. Balaya and S. Devaraj, Tuning the Capacitance Properties of Nanocrystalline MnCO3 by the Effect of a Carbonizing Agent, *J. Electrochem. Soc.*, 2018, **165**(9), A1865–A1873.
7 P. V. Vardhan, M. B. Idris, V. Ramanathan and S. Devaraj, Electrodeposited MnCO3 as a High Performance Electrode Material for Supercapacitor, *ChemistrySelect*, 2018, **3**(24), 6775–6778.
8 Y. A. Kumar, R. M. N. Kalla, T. Ramachandran, A. M. Fouda, H. Hegazy, M. Moniruzzaman and J. Lee, Mxene Mastery: Transforming Supercapacitors through Solid-Solution Innovations, *J. Ind. Eng. Chem.*, 2024, 216–233.
9 K. V. C. Mouli, R. M. N. Kalla, T. Ramachandran, Y. A. Kumar, M. Moniruzzaman and J. Lee, Cutting-Edge Advancements in HOFs-Derived Materials for Energy Storage Supercapacitor Application, *Int. J. Hydrogen Energy*, 2024, **90**, 1–24.
10 M. B. Idris, B. B. Mamba and F. Xolile, Construction of Quasi-Solid-State Supercapacitor with Enhanced High Energy Density Based on Carbon-Rich Graphitic Carbon Nitride and PVA-H2SO4 Gel Polymer Electrolyte, *Diam. Relat. Mater.*, 2025, **160**, 113052, DOI: 10.1016/j.diamond.2025.113052.
11 M. Z. Musa, G. Mukhtar, H. Aliyu, S. Nuhu, H. Abba, A. M. Mohammed, S. Nasir, N. Mansir and M. B. Idris,

Synthesis and Characterization of Nitrogen-Doped Reduced Graphene Oxide for Supercapacitor Application, *Dutse J. Pure Appl. Sci.*, 2025, **11**(1a), 123–131.

12 M. B. Idris, G. Sakthivel and S. Devaraj, Textural Properties Dependent Supercapacitive Performances of Mesoporous Graphitic Carbon Nitride, *Mater. Today Energy*, 2018, **10**, 325–335, DOI: 10.1016/j.mtener.2018.10.012.

13 M. B. Idris and S. Devaraj, Few-Layered Mesoporous Graphitic Carbon Nitride: A Graphene Analogue with High Capacitance Properties, *New J. Chem.*, 2019, **43**(29), 11626–11635.

14 T. Ramachandran, H. Butt, L. Zheng and M. Rezeq, A Review of 2D Metal Boride-Derived Nanostructures: From Synthesis to Energy Storage and Conversion Applications, *J. Energy Storage*, 2024, **99**, 113425.

15 J. Lee, P. Srimuk, S. Fleischmann, X. Su, T. A. Hatton and V. Presser, Redox-Electrolytes for Non-Flow Electrochemical Energy Storage: A Critical Review and Best Practice, *Prog. Mater. Sci.*, 2019, **101**, 46–89.

16 P. Bharathidasan, M. B. Idris, D.-W. Kim, S. Sivakkumar and S. Devaraj, Exploiting the Chemistry of Redox Active Compounds to Enhance the Capacitance of Reduced Graphene Oxide, *FlatChem*, 2019, **15**, 100108.

17 S. Sundriyal, V. Shrivastav, H. Kaur, S. Mishra and A. Deep, High-Performance Symmetrical Supercapacitor with a Combination of a ZIF-67/rGO Composite Electrode and a Redox Additive Electrolyte, *ACS Omega*, 2018, **3**(12), 17348–17358.

18 B. Akinwolemiwa, C. Peng and G. Z. Chen, Redox Electrolytes in Supercapacitors, *J. Electrochem. Soc.*, 2015, **162**(5), A5054.

19 J. Park, V. Kumar, X. Wang, P. S. Lee and W. Kim, Investigation of Charge Transfer Kinetics at Carbon/Hydroquinone Interfaces for Redox-Active-Electrolyte Supercapacitors, *ACS Appl. Mater. Interfaces*, 2017, **9**(39), 33728–33734.

20 G. Arumugam, B. Chettiannan, S. Mathan, M. Selvaraj, M. A. Assiri and R. Rajendran, Better Understanding of Redox Additives in Aqueous Electrolyte for Electrochemical Supercapacitors, *J. Energy Storage*, 2025, **121**, 116595.

21 C. Jin, T. Liu, O. Sheng, M. Li, T. Liu, Y. Yuan, J. Nai, Z. Ju, W. Zhang and Y. Liu, Rejuvenating Dead Lithium Supply in Lithium Metal Anodes by Iodine Redox, *Nat. Energy*, 2021, **6**(4), 378–387.

22 J. Lei, Y. Yao, Z. Wang and Y.-C. Lu, Towards High-Areal-Capacity Aqueous Zinc–Manganese Batteries: Promoting MnO 2 Dissolution by Redox Mediators, *Energy Environ. Sci.*, 2021, **14**(8), 4418–4426.

23 C. Prehal, H. Fitzek, G. Kothleitner, V. Presser, B. Gollas, S. A. Freunberger and Q. Abbas, Persistent and Reversible Solid Iodine Electrodeposition in Nanoporous Carbons, *Nat. Commun.*, 2020, **11**(1), 4838.

24 M. B. Idris and D. Sappani, Unveiling Mesoporous Graphitic Carbon Nitride as a High Performance Electrode Material for Supercapacitors, *ChemistrySelect*, 2018, **3**(40), 11258–11269.

25 M. B. Idris and S. Devaraj, Mesoporous Graphitic Carbon Nitride Synthesized Using Biotemplate as a High-Performance Electrode Material for Supercapacitor and Electrocatalyst for Hydrogen Evolution Reaction in Acidic Medium, *J. Energy Storage*, 2019, **26**, 101032, DOI: 10.1016/j.est.2019.101032.

26 D. Jiang, Q. Xu, S. Meng, C. Xia and M. Chen, Construction of Cobalt Sulfide/Graphitic Carbon Nitride Hybrid Nanosheet Composites for High Performance Supercapacitor Electrodes, *J. Alloys Compd.*, 2017, **706**, 41–47.

27 Q. Chen, Y. Zhao, X. Huang, N. Chen and L. Qu, Three-Dimensional Graphitic Carbon Nitride Functionalized Graphene-Based High-Performance Supercapacitors, *J. Mater. Chem. A*, 2015, **3**(13), 6761–6766.

28 B. Guan, Q. Y. Shan, H. Chen, D. Xue, K. Chen and Y. X. Zhang, Morphology Dependent Supercapacitance of Nanostructured NiCo2O4 on Graphitic Carbon Nitride, *Electrochim. Acta*, 2016, **200**, 239–246.

29 R. Gonçalves, T. M. Lima, M. W. Paixão and E. C. Pereira, Pristine Carbon Nitride as Active Material for High-Performance Metal-Free Supercapacitors: Simple, Easy and Cheap, *RSC Adv.*, 2018, **8**(61), 35327–35336.

30 Y. Cui, J. Zhang, G. Zhang, J. Huang, P. Liu, M. Antonietti and X. Wang, Synthesis of Bulk and Nanoporous Carbon Nitride Polymers from Ammonium Thiocyanate for Photocatalytic Hydrogen Evolution, *J. Mater. Chem.*, 2011, **21**(34), 13032–13039.

31 A. Thomas, A. Fischer, F. Goettmann, M. Antonietti, J.-O. Müller, R. Schlögl and J. M. Carlsson, Graphitic Carbon Nitride Materials: Variation of Structure and Morphology and Their Use as Metal-Free Catalysts, *J. Mater. Chem.*, 2008, **18**(41), 4893–4908.

32 D. H. Park, K. Lakhi, K. Ramadass, M. K. Kim and A. Vinu, Nitrogen-Rich Mesoporous Carbon Nitrides for CO2 Capture and Conversion, *Abstr. Pap. Am. Chem. Soc.*, 2017, 253.

33 M. B. Idris, T. Subramaniam and D. Sappani, Tailoring the Electrocatalytic Activity of Mesoporous Graphitic Carbon Nitride towards Hydrogen Evolution Reaction by Incorporation of Amorphous Carbon, *Diam. Relat. Mater.*, 2022, **129**, 109359.

34 M. B. Idris and S. Devaraj, Tuning the Chemical Composition, Textural and Capacitance Properties of Mesoporous Graphitic Carbon Nitride, *Electrochim. Acta*, 2019, **303**, 219–230, DOI: 10.1016/j.electacta.2019.02.081.

35 A. Vinu, K. Ariga, T. Mori, T. Nakanishi, S. Hishita, D. Golberg and Y. Bando, Preparation and Characterization of Well-Ordered Hexagonal Mesoporous Carbon Nitride, *Adv. Mater.*, 2005, **17**(13), 1648–1652.

36 K. S. Lakhi, W. S. Cha, S. Joseph, B. J. Wood, S. S. Aldeyab, G. Lawrence, J. H. Choy and A. Vinu, Cage Type Mesoporous Carbon Nitride with Large Mesopores for CO_2 Capture, *Catal. Today*, 2015, **243**, 209–217, DOI: 10.1016/j.cattod.2014.08.036.

37 M. Ntozonke, M. B. Idris, K. E. Sekhosana, M. A. Kebede and X. Fuku, The Role of Carbon-based Nanomaterials as Cocatalysts in Enhancing the Photocatalytic Hydrogen Production: A Review, *ChemistrySelect*, 2025, **10**(22), e05612.

38 S. Nuhu, A. M. Mohammed, M. Z. Musaa, H. Aliyua, H. Abbab, G. Mukhtard, A. Ibrahim, N. Mansir and

M. B. Idrisa, Solvothermal Synthesis of Nickel-Based Metal-Organic Frameworks for Supercapacitor Application, *Dutse J. Pure Appl. Sci.*, 2025, **11**(1a), 114–122.

39 H. Abba, M. Ladan, H. Musa, I. T. Siraj, A. M. Yamani, A. S. Muhammad, N. M. Kwalam, A.-R. A. Abdul, A. A. Muhammad and S. Habibu, Investigating the Bifunctional Electrocatalytic Activity of Nickel Oxide/Nitrogen-Doped Reduced Graphene Oxide Nanocomposite for Zinc-Air Battery Application, *J. Solid State Electrochem.*, 2024, 1–11.

40 M. Cao, X. Zhang, J. Qin and R. Liu, Enhancement of Hydrogen Evolution Reaction Performance of Graphitic Carbon Nitride with Incorporated Nickel Boride, *ACS Sustain. Chem. Eng.*, 2018, **6**(12), 16198–16204.

41 B. Arkhurst, R. Guo, G. B. Rokh and S. L. I. Chan, *Hydrogen Storage Properties of Graphitic Carbon Nitride Nanotube Synthesized by Mix-Grind Technique*, Springer, 2023, pp 223–231.

42 A. Bafekry, M. Faraji, N. N. Hieu, A. B. Khatibani, M. M. Fadlallah, D. Gogova and M. Ghergherehchi, Tunable Electronic Properties of Porous Graphitic Carbon Nitride (C_6N_7) Monolayer by Atomic Doping and Embedding: A First-Principle Study, *Appl. Surf. Sci.*, 2022, **583**, 152270.

43 B. Antil, L. Kumar, M. R. Das and S. Deka, N-Doped Graphene Modulated N-Rich Carbon Nitride Realizing a Promising All-Solid-State Flexible Supercapacitor, *J. Energy Storage*, 2022, **52**, 104731.

44 M. B. Idris, G. H. Sai, D. Hemalatha, G. Sakthivel and S. Devaraj, The Effect of Phosphorous Doping on the Composition and Capacitance Properties of Mesoporous Graphitic Carbon Nitride, *J. Electrochem. Soc.*, 2019, **166**(12), A2409–A2418, DOI: 10.1149/2.0311912jes.

45 K. S. W. Sing, Reporting Physisorption Data for Gas/Solid Systems with Special Reference to the Determination of Surface Area and Porosity (Recommendations 1984), *Pure Appl. Chem.*, 1985, **57**(4), 603–619.

46 E. Alwin, M. Zieliński, A. Suchora, I. Gulaczyk, Z. Piskuła and M. Pietrowski, High Surface Area, Spongy Graphitic Carbon Nitride Derived by Selective Etching by Pt and Ru Nanoparticles in Hydrogen, *J. Mater. Sci.*, 2022, **57**(33), 15705–15721.

47 T. Sano, S. Tsutsui, K. Koike, T. Hirakawa, Y. Teramoto, N. Negishi and K. Takeuchi, Activation of Graphitic Carbon Nitride (gC 3 N 4) by Alkaline Hydrothermal Treatment for Photocatalytic NO Oxidation in Gas Phase, *J. Mater. Chem. A*, 2013, **1**(21), 6489–6496.

48 H.-Y. Xu, L.-C. Wu, H. Zhao, L.-G. Jin and S.-Y. Qi, Synergic Effect between Adsorption and Photocatalysis of Metal-Free g-C3N4 Derived from Different Precursors, *PLoS One*, 2015, **10**(11), e0142616.

49 R. Moodakare, B. Sahoo, N. Bharadishettar, M. R. Rahman, M. Muhiuddin and U. B. K, Synthesis and Characterization of N-Doped Reduced Graphene Oxide for the Supercapacitor Application, *J. Mater. Sci. Mater. Electron.*, 2025, **36**(10), 616.

50 H. Khanari, M. S. Lashkenari and H. Esfandian, Polythiophene/Nitrogen-Doped Reduced Graphene Oxide Nanocomposite as a Hybrid Supercapacitor Electrode, *Int. J. Hydrogen Energy*, 2024, **68**, 27–34.

51 I. Ishita, P. Sahoo, P. K. Sow and R. Singhal, Unlocking the Potential of KI as Redox Additive in Supercapacitor through Synergistic Enhancement with H2SO4 as a Co-Electrolyte, *Electrochim. Acta*, 2023, **451**, 142286, DOI: 10.1016/j.electacta.2023.142286.

52 A. Platek-Mielczarek, E. Frackowiak and K. Fic, Specific Carbon/Iodide Interactions in Electrochemical Capacitors Monitored by EQCM Technique, *Energy Environ. Sci.*, 2021, **14**(4), 2381–2393.

53 A. J. Bard, L. R. Faulkner and H. S. White, *Electrochemical Methods: Fundamentals and Applications*, John Wiley & Sons, 2022.

54 M. B. Idris, B. B. Mamba and F. Xolile, Facile Synthesis of Nickel Oxide/Delaminated Boron Composite with an Enhanced Electrocatalytic Activity Towards the Oxygen Evolution Reaction in Alkaline Medium, *Electrocatalysis*, 2025, 1–10.

55 M. B. Idris, B. B. Mamba and F. Xolile, Palladium-Integrated MnO2/Delaminated Boron Nanocomposite as an Efficient Electrocatalyst toward Ethanol Electrooxidation in an Alkaline Medium, *Ionics*, 2025, 1–15.

56 T. M. Patil, A. H. Patil, M. Krishnaiah, D. Mishra, A. Kumar, N. Kumar, V. D. Chavan, D.-K. Kim, S. B. Patil and S. B. Sadale, Enhanced Electrochemical Performance of CuCo2O4 Nanowire Arrays Based Solid-State Symmetric Supercapacitor by K3 [Fe (CN) 6] Redox Additive Electrolyte, *J. Energy Storage*, 2023, **63**, 106945.

57 N. Zhao, H. Fan, M. Zhang, J. Ma, Z. Du, B. Yan, H. Li and X. Jiang, Simple Electrodeposition of MoO3 Film on Carbon Cloth for High-Performance Aqueous Symmetric Supercapacitors, *Chem. Eng. J.*, 2020, **390**, 124477.

58 P. Zhang and H. He, NiCo2S4 Nanosheet-Modified Hollow Cu-Co-O Nanocomposites as Asymmetric Supercapacitor Advanced Electrodes with Excellent Performance, *Appl. Surf. Sci.*, 2019, **497**, 143725.

59 R. S. Nicholson, Theory and Application of Cyclic Voltammetry for Measurement of Electrode Reaction Kinetics, *Anal. Chem.*, 1965, **37**(11), 1351–1355.

60 R. Agarwal, The Nicholson Method of Determination of the Standard Rate Constant of a Quasireversible Redox Couple Employing Cyclic Voltammetry: Everything One Needs to Know!, *ACS Electrochem.*, 2025, **1**, 1885–1894.

61 A. Kumar, B. N. Mahanty, A. Rawat, R. Muhammad, R. K. Panigrahi, D. Pradhan and P. Mohanty, Transition-Metal-Substituted Nanoporous Manganese Ferrites Mn0. 95M0. 05Fe2O4 (M: Co, Cu, and Zn) as Electrode Materials for High-Performance Supercapacitors in Redox-Active Nonaqueous Electrolytes, *Energy Fuels*, 2023, **37**(9), 6810–6823.

62 M. Skunik-Nuckowska, P. Rączka, J. Lubera, A. A. Mroziewicz, S. Dyjak, P. J. Kulesza, I. Plebankiewicz, K. A. Bogdanowicz and A. Iwan, Iodide Electrolyte-Based Hybrid Supercapacitor for Compact Photo-Rechargeable

Energy Storage System Utilising Silicon Solar Cells, *Energies*, 2021, **14**(9), 2708.

63 A. Klimek, M. Tobis and E. Frackowiak, Effect of a Buffer/Iodide Electrolyte on the Performance of Electrochemical Capacitors, *Green Chem.*, 2024, **26**(11), 6684–6695.

64 M. Maher, S. Hassan, K. Shoueir, B. Yousif and M. E. A. Abo-Elsoud, Activated Carbon Electrode with Promising Specific Capacitance Based on Potassium Bromide Redox Additive Electrolyte for Supercapacitor Application, *J. Mater. Res. Technol.*, 2021, **11**, 1232–1244.

65 N. Liang, X. Wu, Y. Lv, J. Guo, X. Zhang, Y. Zhu, H. Liu and D. Jia, A Graphdiyne Oxide Composite Membrane for Active Electrolyte Enhanced Supercapacitors with Super Long Self-Discharge Time, *J. Mater. Chem. C*, 2022, **10**(7), 2821–2827.